Helene's surface properties from a photometric multi-wavelength analysis

E. Royer[1], A. Hendrix[1], J. Elliott[2], L. Esposito[2], C. Howett[3], L. Spilker[4]
1 – Planetary Science Institute (PSI), Tucson, AZ
2 – Laboratory for Atmospheric and Space Physics (LASP), Boulder, CO
3 – University of Oxford, UK
4 – Jet Propulsion Laboratory (JPL), la Canada, CA

Abstract

On January 31, 2011, the remote-sensing instruments onboard the Cassini spacecraft (UVIS (Ultraviolet Imaging Spectrograph; ISS (Imaging Science Subsystem); VIMS (Visual and Infrared Mapping Spectrometer) and CIRS (Composite Infrared Spectrometer)) observed Helene, Dione's leading Lagrangian moon. We report here on the photometric characteristics of Helene between 0.11 μm and 5.2 μm. We find that Helene's spectrum is dominated by the signature of water-ice and we retrieve a grain size of 3.4 μm in the ultraviolet. At all wavelengths, Helene shows signs of being a relatively fresh surface less affected by space weathering effects than other observed surfaces in the Saturn system. We present the first phase curve of Helene at 0.61 μm and place our ultraviolet and near-IR results in a wider spectral context toward a better understanding of Helene's surface evolution. Previous studies suggested that either a recent impact on Helene or an asymmetric flux of E-ring particles could explain the satellite high surface brightness (Hedman et al., 2020). Results from this study favor the impactor hypothesis to explain Helene's photometric behavior.

Introduction

The icy satellites of Saturn are among the brightest surfaces in the Solar System, and at Saturn exogenic bombardment by the E-ring particles is the primary agent to brighten icy surfaces (Buratti et al., 1998; Buratti and Veverka, 1984; Nelson et al., 1987; Verbiscer et al., 2007). This paper focuses on Helene, one of Dione's co-orbital moons. Both Dione and Helene orbit at 6.26 radii from Saturn. Helene is located at Dione's leading Lagrangian point L4 and is non-spherical in shape (22.6 km by 19.5 km by 13.3 km diameter) (Thomas and Helfenstein, 2019; Thomas et al., 2013). Due to its small size and low magnitude (m = 18.5) Helene is difficult to study from the Earth, but the Cassini Imaging Science Subsystem (ISS) obtained global coverage with some images at up to 40 m/pixel spatial resolution. These images showed that Helene is covered in a 10-20 m thick regolith that is being eroded at scarps (Thomas et al. 2018). Umurhan et al. (2015) reported that non-steady state processes are most likely the cause of downslope material movements, with rapid coverings that are followed by the downslope removal of additional loose material.

Helene's spectroscopic properties differ from those of Dione (Verbiscer et al., 2007, 2018; Filacchione et al. 2012) since Dione exhibits significant leading/trailing asymmetry, where the Leading Hemisphere (LH) is brighter than the Trailing Hemisphere (TH) and dark material(s) preferentially deposits on the TH (Buratti and Veverka, 1984, Royer and Hendrix, 2014, Verbiscer et al., 2018). At Helene, Filacchione et al. (2012) used visible and infrared wavelengths as observed by Cassini's Visual and Infrared Mapping Spectrometer (VIMS) to report that the surface is bluer, and hence contains much fresher water ice than Dione. Hedman et al. (2020), using Cassini ISS data, also showed that Helene is substantially brighter than Dione, which may be due to an asymmetric flux of E ring particles or recent collisions with large impactors. Umurhan et al (2021) performed a geomorphological analysis and modeling of Helene, based on ISS images, and concluded that Helene's cratered surface has been heavily modified by mass flows. The preferential location of long mass flows on the leading side of Helene suggests the accumulation of exogenous granular ice as a major source of the mobile material. Estimated rates of deposition derived

from the current *E*-ring system are very low, suggesting alternative sources of granular ice such as i) cryovolcanism, ii) impact-generated debris from Dione or Tethys, or iii) a catastrophic recent event in the inner satellite system of Saturn, in agreement with the Hedman et al. (2020) impactor hypothesis.

All previous studies were made within a specific wavelength domain, either visible or infrared, telling only part of the story. We are reporting here on the first ultraviolet (UV) results on Helene, which probes the upper-most layer of its regolith. By combining UV, VIS and IR data (both from the VIMS data analyzed here and the CIRS data analyzed in a companion paper, Howett and Royer (2021)), our study covers a wide wavelength range. This enables us to tell a more complete story than the previous analysis (e.g. Filacchione et al., 2012; Hedman et al., 2020; Umurhan et al., 2021) that focused on a single wavelength domain.

Observations

In this study, we focus on a subset of Cassini observations, where the four remote-sensing instruments (UVIS, ISS, VIMS and CIRS) were observing Helene simultaneously. This ensures that all spectra are taken under similar illumination conditions and reduces the need for photometric correction to cross-calibrate observations.

The UVIS instrument, (c.f. Esposito et al., 2004), is composed of two-dimensional CODACON detectors that provide simultaneous spectral and one-dimensional spatial images. The far-UV channel covers wavelengths from 111.5 nm to 191.2 nm. The detector format is 1024 spectral pixels by 64 spatial pixels. Each spectral pixel is 0.25 mrad and each spatial pixel is 1.0 mrad projected on the sky. Our study focuses on observations using the low-resolution slit, giving a spectral resolution of 0.48 nm and a spatial Field of View (FOV) of 1.5 mrad in the spectral dimension.

The ISS instrument consists of two cameras, the narrow angle camera (NAC) and the wide-angle camera (WAC) (Porco et al., 2004). Both cameras use a 1024 × 1024- element charge-coupled device (CCD) array detector. We exclusively used data from NAC, which has an image scale of 5.9907 μrad/pixel. In-flight calibration of the cameras is described by West et al. (2010). Each camera contains two filter wheels; the filter coverage for the NAC, including the 610 nm filter, is shown in Porco et al. (2004).

The VIMS instrument (Brown et al., 2004) covers the 0.35– 5.1 μm spectral range by imaging a 1.8 x 1.8° FOV with 64 pixels. The experiment consists of two imaging spectrometers (VIS and IR) observing the same field of view in two spectral ranges. VIMS-V is the Italian-made imaging spectrometer covering the 0.35–1.05 μm range in 96 spectral channels and spatial resolutions of 500 × 500 (nominal) or 166 × 166 (high resolution) μrad/pixel (Miller et al., 1996). VIMS-IR is the US-made channel covering the 0.8–5.1 μm spectral range with 256 spectral channels and spatial resolutions of 500 (nominal) or 500 × 250 (high resolution) μrad/pixel.

The Cassini's Composite Infrared Spectrometer (CIRS) observations will not be explicitly analyzed in this paper, as retrieving the I/F ratio does not make physical sense at the CIRS wavelengths above about 10 microns because Helene's surface thermally emits, instead of reflecting the sunlight at those wavelengths. However, the UVIS, ISS and VIMS observations will be interpreted in light of a companion paper (Howett and Royer, 2021) exclusively focused on the CIRS results at Helene.

Date of observation For Helene observation		Phase angle range (°)	Distance from spacecraft (km)	Averaged angular diameter (°)	Sub-spacecraft Longitude (°W)	Sub-spacecraft Latitude (°)	Start Time of observation of each instrument	End Time of observation of each instrument
Jan 31, 2011 (2011_031)	UVIS	36.8 – 66.8	39613.	0.05	136.	-3.	10:46:09.157	11:46:09.157
	ISS	88.2 to 62.5	27711.	0.065	94.	-4.	10:21:25.307	10:52:06.197
	VIMS	33.2 to 39.3	49891.	0.035	155.	-2.	11:38:51.749	11:59:22.024

Table 1. List of Helene's observations performed with the UVIS, ISS and VIMS instruments on January 31, 2011. Information regarding the CIRS parameters on the same day of observation (2011_031) can be found in Howett and Royer (2021).

Detailed information regarding the January 31, 2011 Helene observations analyzed in this paper is presented in Table 1. Geometric parameter values are averaged over the span of each observation.

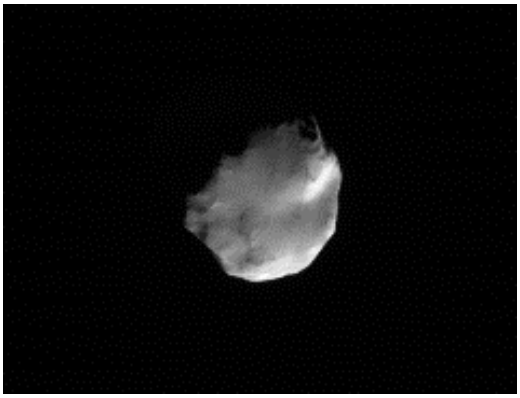

Fig 1. Image of Helene, obtained by the Cassini ISS-NAC instrument using its clear filters (in mode "CL1", "CL2"). On January 31, 2011, ISS NAC clear filter ISS image co-iss-n1675163665 was taken at 2011-01-31T10:21:26 at a sub-spacecraft location of 94° W and 4° S.

Co-added spectra from UVIS, ISS and VIMS presented in Figure 2 span wavelengths 110 to 5000 nm, and are normalized at 550nm, which is the wavelength at which Helene's spectrum exhibits its highest reflectance value. UVIS resolution was degraded to match VIMS resolution. ISS data consists of discrete data points at specific filter wavelengths and reflectance has been interpolated over the wavelength range of ISS. As shown in Figure 2a, one major data gap in wavelength is present from 190 nm to about 350 nm, between the UVIS and ISS/VIMS datasets. However, no spectral features of importance are expected in this gap, and the reflectance is anticipated to increase steadily within this gap in wavelengths, as demonstrated by the Hubble Space Telescope (HST) Space Telescope Imaging Spectrometer (STIS) and the Faint Object Spectrograph (FOS) data, which fill in the spectral gap between ISS and UVIS, where HST data are available (Hendrix et al. (2018)).

The main identifiable spectral features are water-ice: in the ultraviolet, the water-ice absorption edge is centered around 165 nm (Hendrix and Hansen, 2008); in the infrared, the most diagnostic absorption bands of pure water-ice absorption bands are located at 1.05, 1.25, 1.5, 2.0 and 3.0 μm. Figures 2b, c and d display zoom-in views of the spectrum at wavelength ranges 150-190nm, 350-1500nm and 100-900nm, respectively. Figure 2b shows the UVIS data. The spectrum is dark in the UV and the signal to noise ratio (SNR) is low at wavelength shortward of 160nm. Aside from the water-ice absorption edge, an absorption feature is detected around 185nm. The 185nm absorption feature, still to be identified, has been seen in the Cassini-UVIS data on most of the icy satellites of Saturn and the rings as well (Royer et al., 2019, Hendrix and Hansen, 2008, Elowitz et al. 2021). Figure 2c spans wavelengths in common between the ISS and VIMS instrument and show that reflectance measurements are in agreement between the two instruments. The reflectance spectrum is mostly flat across the 350-900 nm wavelength range and tilts downward longward of 900nm, mostly due to the presence of pure water-ice. Figure 2d emphasizes how flat and devoid of diagnostic spectral features the reflectance spectrum is in the visible/near-IR between 350 and 900nm.

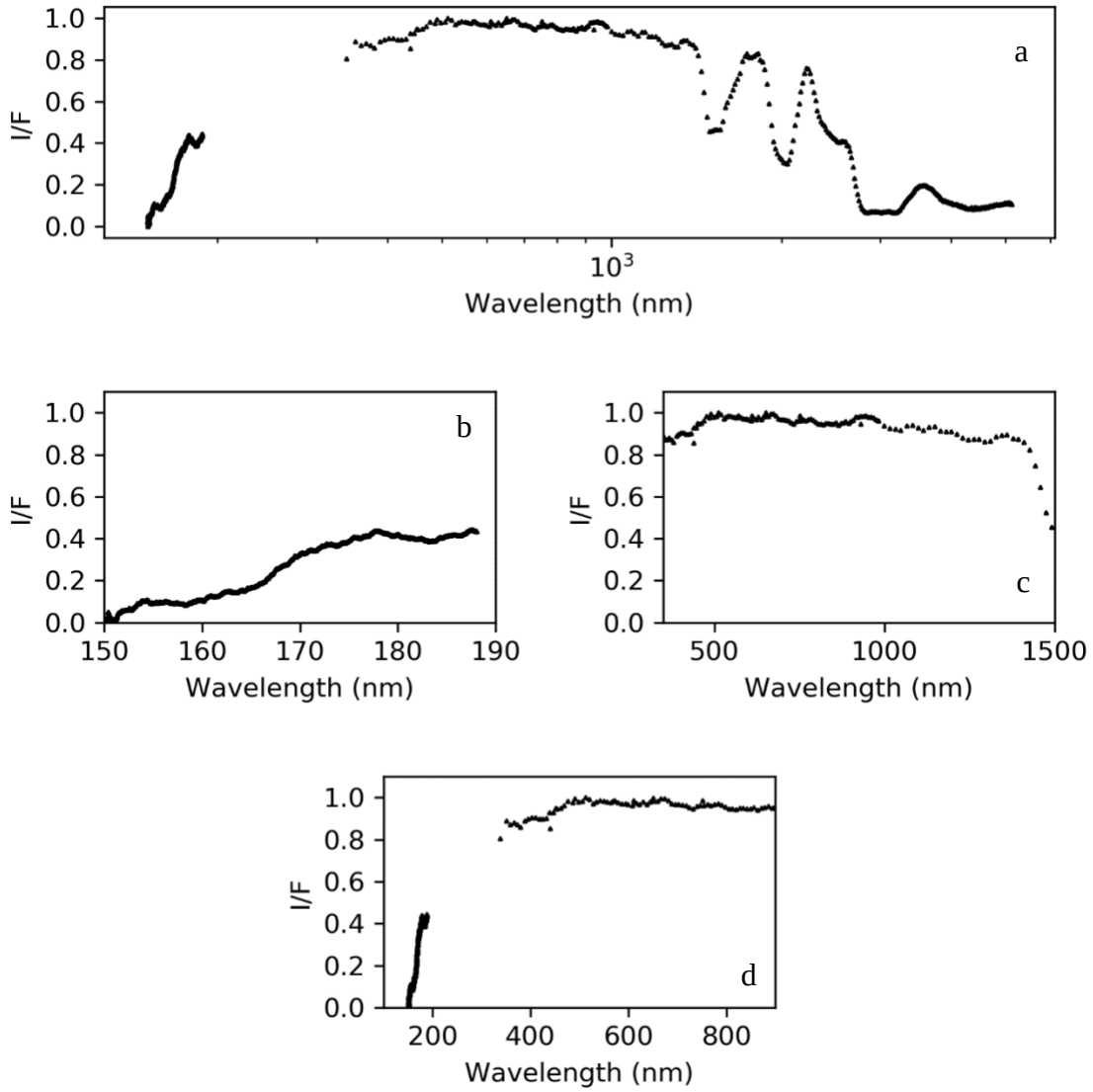

Fig 2. Helene spectrum on January 31, 2011, normalized to the reflectance at 550 nm. The spectrum is a combination of the UVIS, ISS and VIMS data including wavelengths from 115nm up to 5200nm, as shown in Panel a. Panel b show the UVIS spectrum. Panel c shows the wavelength range 350-1500nm, including data from ISS and VIMS instruments. Panel d shows the wavelength range 115-900nm, representative of the UV-VIS-Near IR.

Photometric analysis

We performed several photometric analyses using all data available for photometry. The ISS dataset provided enough data to attempt a phase curve analysis at 610nm, while there are not enough data points in the ultraviolet to create a phase curve, but only to perform compositional modeling and grain size estimates.

Ultraviolet photometry

We modeled the UVIS spectrum of Helene with the Hapke model (Hapke 2012), using pure water-ice optical constants from Warren and Brandt (2008). As seen on Figure 3, pure water-ice reproduces the water-ice absorption edge centered around 165nm, but does not fit the 185nm absorption feature, suggesting

the presence of one or several additional contaminant(s) to the water-ice at Helene. Moreover, the low reflectance in the ultraviolet domain compared to visible wavelengths is in itself indicative of an absorbing species in the UV.

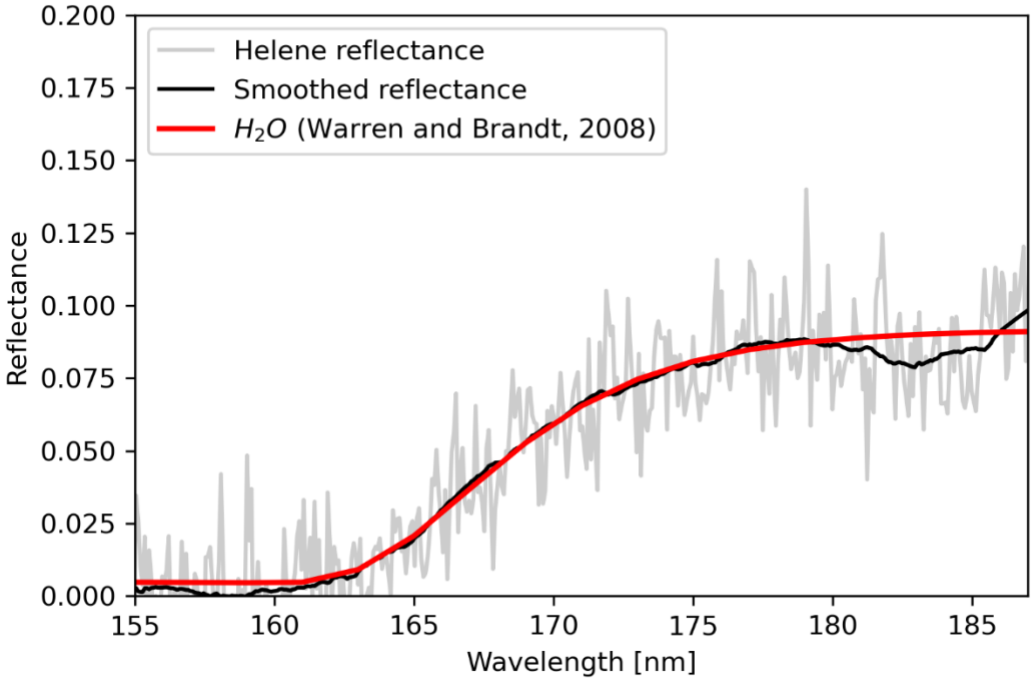

Fig 3. Hapke pure water-ice model of Helene UVIS spectrum of January 11, 2011. The grey line represents the original reflectance spectrum, while the black line is the smoothed reflectance. Data were smoothed using the Savitzky-Golay filter with window length 101 and polynomial order 3. The pure water-ice model is indicated in red.

We retrieved a best-fit water-ice grain size of 3.4 +/- 0.4 μm in the UV 150-190 nm wavelength range for Helene's LH, by fitting the Hapke model to the position of the water ice absorption edge. For comparison, Filacchione et al. (2012) reported grain diameters of about 10–20 μm across the leading hemisphere of Dione and less than 10 μm across the trailing hemisphere of Dione, using VIMS data between 0.8 and 5 μm. They also found increasing grain sizes with increasing wavelengths with grain sizes of about 11 μm at 1.25 μm; between 14 μm and 1.15 cm at 1.5 μm and between 27 μm and 0.88 cm at 2.00 μm. Our value of 3.4 +/- 0.4 μm in the UV 150-190 nm wavelength range would indicate a change in the grain size distribution with depth compatible with material compaction, assuming that VIMS observations of Helene would provide the same grain sizes as the VIMS observations of Dione.

Visible/near-IR photometry

The ISS instrument acquired enough data with the 610 nm filter to build a phase curve over a phase angle range from 20°-100°, although the range of longitudes observed was insufficient to photometrically correct the phase curve with a rotational curve, as most data points belong to the Leading Hemisphere (See Tables A.1 and A.2 in Appendix). We choose the 610 nm filter because Helene's spectrum is brightest around 610 nm and the signal to noise ratio (SNR) is thus highest. Therefore, the measured reflectance allows one to robustly retrieve the single scattering albedo (ω) and the Henyey-Greenstein phase function parameters (b and c), using a shadow-hiding Hapke model (Hapke 2012). We first used the same methods and Hapke model as in Hendrix et al. (2005) and Royer and Hendrix (2014), using only the Shadow Hiding process (SHOE – parameters B_0 and h) to fit the Helene and Dione data at 610nm. We initially decided to

not account for the coherent-backscatter process (CBOE) because it requires phase angles smaller than 2° to be constrained. Information collected on the opposition effect at Helene is thus of limited significance, given the lack of data a low phase angle (less than 20°). Additionally, the macroscopic roughness necessitates large phase angles above 100° to be robustly constrained and thus the results here should be treated with caution. The Hapke model is widely known for the non-uniqueness of its solution. We selected what we expect to be the most realistic set of Hapke parameters fitting the phase curves and spectra of Helene and Dione, based on previous analysis of similar objects.

Previously published estimates of the mean visual geometric albedos (HST V-band) at true opposition were found to be 0.55 +/- 0.15 for Dione and 0.65 +/- 0.05 for Helene (Burns, 1986). Updated values measured by HST's WFPC2 in the F555W filter at 550nm were reported at 0.998 +/- 0.004 for Dione and 1.67 +/- -.20 for Helene (Verbiscer et al., 2007). However, Helene value should be treated with caution because the lightcurve was not available to correct the data from longitudinal effect. We are considering the measured Verbiscer et al. (2007) updated values for Helene and Dione in our study. Both datasets at Helene and Dione lack good coverage at phase angle lower than 2 degrees. However , the visual geometric albedo measured at 550nm can be used as a proxy for the visual geometric albedo at 610nm because the reflectance is relatively flat at those wavelengths, indicating that the visual geometric albedo at 550nm can be considered to be representative of the geometric albedo at 610nm, within error bars. Adding the Verbiscer et al. (2007) value provides a mean to test for the contribution of coherent backscattering to the opposition effect. The coherent backscattering opposition effect (CBOE) is mainly known as the mechanism that produces a narrow opposition spike in solar phase curves at phase angles smaller than 2 degrees. Due to a strong dependence of the opposition spike caused by CBOE on the albedo of the surface (i.e., the higher the albedo is, the sharper the slope of the CBOE becomes), the spike is expected to be steeper for less absorbing materials.

The single-scatter albedo ω and the Henyey-Greenstein b and c terms are the parameters most robustly constrained by the Hapke model. In this study we used the two parameters Henyey–Greenstein function (2P-HG) after Domingue et al. (1991), which has been widely used in the literature for icy satellite photometry and will facilitate comparisons of our results.

Model results from this study are presented in Figure 4 and Table 2, where we compare Helene ISS data on the LH with Dione FUV published results (Royer and Hendirx, 2014) and ISS data of Dione's leading hemisphere. Figure 4 shows the Helene and Dione phase curves along with two Hapke best-fit models. For each satellite, the solid line represents the Hapke model including only the Shadow Hiding Opposition Effect (SHOE) to reproduce the 610 nm phase curve. The dashed line represents the Hapke model with the addition of the CBOE to the SHOE. On Helene's leading hemisphere, the presence of SHOE only is able to reproduce the previously published value of Helene visual albedo (0.65 +/- 0.05), but does not allow to reproduce the updated value at 1.67 +/- 0.20 measured at 550nm. The inclusion of CBOE is key to be able to fit the model to the visual geometric albedo, indicating the presence of multiple scattering on the surface of Helene at visible wavelengths. The same, but to a lesser extent, is observed for Dione. Dione opposition effect retrievals are mostly constrained by a single data point at 5.5 degrees phase angle. Helene phase curve does not include data points at phase angle lower than 21.6 degrees, which renders challenging the comparison of the opposition effect values between the two satellites.

The single scattering albedo, ω, was found to be above 0.89 in each case (SHOE or SHOE + CBOE) for both Helene and Dione, indicating the presence of relatively pure water-ice. This high value of ω also reflects the likeliness of multiple scattering over single scattering. Table 2 shows that the single scattering albedo at Helene and Dione's leading hemisphere in the visible is significantly higher, by about a factor 2, than the retrieved values for Dione in the ultraviolet at 180 nm. This is consistent with a composition made of mostly water-ice and of multiple-scattering affecting the surface at visible wavelength. The visible/near-IR wavelengths also probe deeper than the far-ultraviolet, and the higher single scattering albedo could reflect a less weathered surface below the layer probed by ultraviolet light.

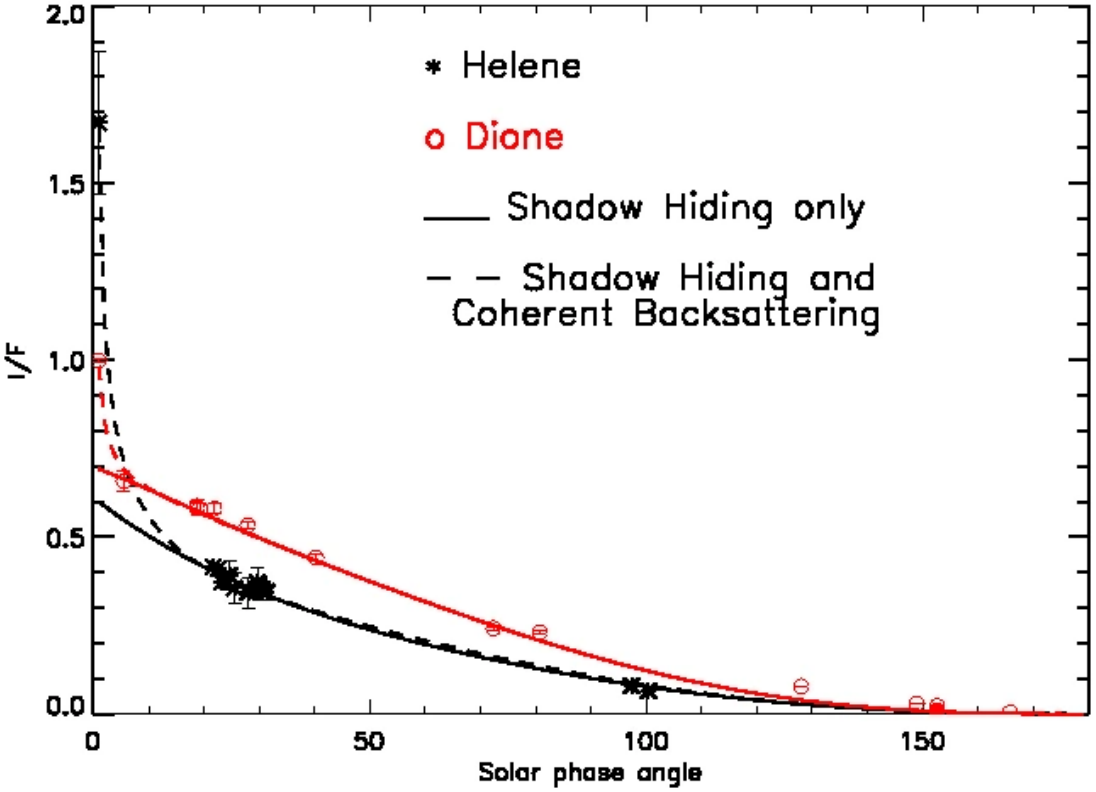

Fig 4. Hapke best-fit of Helene and Dione's LH phase curves at 610nm, using two version of the 2012 Hapke model. The solid line represents the Hapke model which includes the Shadow Hiding process only to reproduce the opposition surge. The dashed line represents the Hapke model including the effect of Shadow Hiding and Coherent Backscattering to reproduce the opposition surge. Helene's data are shown in black with the asterisk symbol. Dione data are shown in red with the circle symbol. The lowest phase angle points ($\alpha < 1°$) for Dione and Helene correspond to phase angle 550 nm and are from Verbiscer et al. (2007), while the rest of the data ($\alpha > 1°$) were obtained by the ISS instrument at 610 nm.

The 2P-HG b parameter represents the amplitude of the scattering lobes. The 2P-HG assumes that the half-widths of the forward and backward scattering lobes are equivalent, and that the relative amplitude varies. The c parameter pertains to the direction of scatter; no forward scattering components have been found in this analysis, only backward-scattering. We found Helene to be less forward scattering than Dione at 180 and 610 nm, while both lobes scatter in the same direction (c = 1). Furthermore, the inclusion of CBOE in the model resulted in a further decrease in the scattering lobe amplitude for Helene's LH.
The B_0 parameter is the amplitude of the shadow-hiding opposition effect and a representation of the transparency of the particles, a value of 1 meaning an opaque particle. Helene's particles, with a value of 0.9 was found to be comparable to what we observed in the UV, while Dione displays more transparent grains than Helene in the visible and than itself in the ultraviolet. The difference in opacity of the particle could inform on the material's compaction processes as the light probes the surface deeper at longer wavelengths. The h parameter is the angular half-width of the shadow-hiding opposition effect, and was found to be the be of equivalent values across Helene and Dione models in the visible, due to large error bars for this parameter. Both Dione and Helene required the addition of CBOE to reach the updated geometric albedo values. However, Helene displays a greater Bc0 value than Dione, which represents the amplitude of the coherent backscattering. The higher Bc0 value at Helene could be triggered by the lack of data points around 5 degrees phase angle.

In Hapke theory, the roughness parameter is representative of the macroscopic roughness with low value indicating smooth surfaces. Roughness values used to model the ultraviolet data were fixed to 20° based on previous studies (Verbiscer 2018, Domingue 1991, Royer and Hendrix, 2014). In this study, we found equivalent values for Helene and Dione roughness with 11° +/- 5.00 in the visible, showing that the surface at Helene and Dione are macroscopically relatively smooth, in agreement with the large-scale appearance of mass flows observed at Helene and the uniform brightness of Dione's LH. Helene is covered in a 10-20 m thick regolith and its cratered surface has been heavily modified by mass flows (Thomas et al., 2013; Umurhan et al., 2021). We remind the reader here that the results regarding the roughness should be treated with caution because it requires good coverage at phase angle higher than 100° and the data obtained by ISS at Helene and by UVIS at Dione are insufficient to well-constraint this parameter.

	ω	b	c	B_0 (SHOE)	h (SHOE)	Bc_0	hc	Roughness (°)
Helene LH at 610 nm SHOE	0.89 +/-0.05	0.35 +/- 0.10	1.00 +/- 0.10	0.90 +/- 0.20	0.24 +/- 0.30	-	-	11.00 +/- 5.00
Helene LH at 610 nm CBOE	0.90 +/-0.05	0.15 +/- 0.10	1.00 +/- 0.10	0.90 +/- 0.20	0.30 +/- 0.30	0.95 +/-0.05	0.04 +/-0.01	11.00 +/- 5.00
Dione LH at 610 nm SHOE	0.99 +/-0.01	0.45 +/- 0.05	1.00 +/- 0.05	0.30 +/- 0.10	0.324 +/- 0.20	-	-	11.00 +/- 5.00
Dione LH at 610 nm CBOE	0.99 +/-0.01	0.43 +/-0.1	1.00 +/- 0.05	0.30 +/-0.10	0.324 +/-0.20	0.87 +/-0.02	0.005 +/-0.01	11.00 +/- 5.00
Dione LH at 180nm (Royer and Hendrix, 2014)	0.484 +/- 0.02	0.35 +/- 0.02	1.00 +/- 0.02	0.95 +/- 0.15	0.457 +/- 0.07	-	-	20.
Dione TH at 180nm (Royer and Hendrix, 2014)	0.211 +/- 0.02	0.44 +/- 0.02	1.00 +/- 0.02	0.95 +/- 0.15	0.505 +/- 0.10	-	-	20.

Table 2. Best fit Hapke parameters for Dione and Helene Leading hemispheres' phase curves at 610nm (this work), in comparison to Dione LH and TH at 180 nm (Royer and Hendrix, 2014).

Discussion

The ωP(0) term, where P(0) is the phase function at zero phase angle, describes the total light scattered from the particles in a regolith, both from internal and surface scattering. Hendrix et al. (2005) linked an increase in the ultraviolet ωP(0) value to the increased amount of bombardment experienced by the satellite surfaces, based on a study of the Galilean satellites. Further results on the icy satellites of Saturn in the ultraviolet also supported this interpretation, with Tethys and Mimas exhibiting higher ωP(0) values than Dione. Helene's ωP(0) average value at 610 nm is 2.13, which falls between Dione's LH (1.5) and Tethys' TH (2.2) ωP(0) values (Royer and Hendrix, 2014). Dione average ωP(0) value at 610nm is 4.5,

which if the current interpretation by Hendrix et al (2005) and Royer and Hendrix (2014) extend in the visible would suggest an heavier amount of E-ring bombardment on Dione LH compare to Helene LH.

Water-ice grain sizes of 3.4 +/- 0.4 μm are required to fit the UV 150-190 nm data. A qualitative comparison between Helene's UV spectrum and Dione's LH and TH disk-integrated UV spectra allows an estimate of how grain sizes changes from one satellite to the other, because the position of the water-ice absorption edge shifts toward shorter wavelength as the grain size decreases. Figure 5 presents normalized FUV spectra of Helene LH, Dione LH and Dione TH. Helene's and Dione LH and TH water-ice absorption edges are all starting around 162.5 nm, indicating similar grain sizes at Helene and Dione for the observed spectra in ultraviolet. Nonetheless, Helene presents a slightly flatter slope of the water-ice spectral edge signature, especially contrasting with Dione LH, suggesting the presence of different absorber(s) or a different regolith structure at Helene. Information shortward 160 nm can be disregarded as the reflectance is very dark and the signal is embedded within the noise. A smaller grain size retrieved from UV data compared to one obtained from visible wavelength could indicate a different porosity or some material compaction with depth.

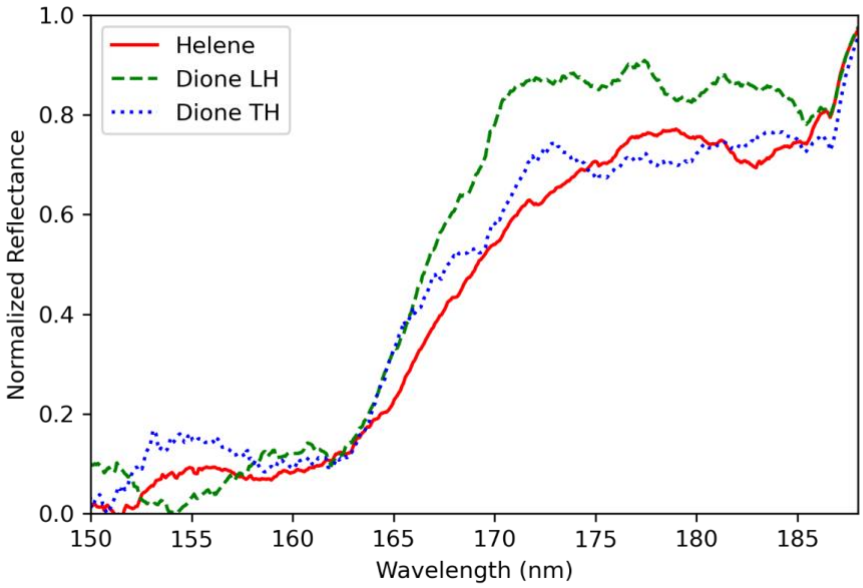

Fig 5. Helene LH UVIS spectrum comparison with Dione LH and TH UVIS spectra. The Helene spectrum is the same as in Figure 3. Dione LH spectrum was taken from observation made on June 25, 2008, at phase angle 7.60° and longitude146.03°. Dione TH hemisphere spectrum was taken from observation made on February 3, 2008, at phase angle 5.45° and longitude 256.64°. All observations are normalized to the maximum value to emphasize spectral differences and data were smoothed using the Savitzky-Golay filter with window length 101 and polynomial order 3.

The UV, visible and near-IR data at Helene shows that Helene's surface has many characteristics in common with the surfaces of the regular icy satellites of Saturn: Helene is among the brightest of the solar system surfaces in the visible domain, its spectrum from ultraviolet to infrared is dominated by the spectral signature of water-ice, but possess a significantly darker reflectance in the ultraviolet, indicating the presence of one or several absorber(s) on the surface. However, Helene exhibits key differences as show by Filacchione et al. (2012) with spectral evidence of bluer hence fresher water-ice on its surface compared to Dione. This work also showed that Helene's water-ice grain size in the ultraviolet is smaller by a factor of at least 2 to Dione's grain sizes retrieved in the infrared. Further analysis of ultraviolet spectra shows Helene and Dione to have similar grain size in the 150-190 nm range, based on the position of the water-ice absorption edge. Further studies beyond the scope of this paper are required to investigate the grain size

evolution of water-ice at Dione with depth to evaluate the effect of compaction or other mechanism on the grain size distribution.

Helene's FUV spectrum displays an additional absorption feature centered around 185 nm. This spectral signature has been previously observed on many other icy satellite and ring spectra in the Saturn system (Hendrix et al., 2008, Royer et al., 2019). More recently, the 185 nm signature has also been detected on Europa using HST data (private communication), opening the way to further compositional investigation. To date, the best datasets to model water-ice in the FUV wavelength range are the Warren (1984) and Warren and Brandt (2008) optical constants. Data were acquired at temperature T = 80 k, which is close to the average Dione's surface temperature (T ~ 87 K) using hexagonal and amorphous crystalline phases. By comparing cubic, hexagonal, and amorphous phases at 77 K, Pipes et al (1974) have demonstrated that the crystalline phase can influence the spectral signature in the FUV and have shown the presence of an absorption band around 185-190 nm. Further laboratory experiments are then needed to determine if the absorption band detected around 185 nm is linked to the water-ice or to a contaminant to the water-ice. If from a contaminant, the absorption could be of exogenic origin since the spectral signature is observed everywhere in the Saturn system. On the contrary, the absorption could also be endogenic in nature, due to a potential radiolytic reaction. The current state of knowledge does not allow conclusion to be drawn on this point. Additionally, the presence of the 185 nm absorption at Helene seems to contradict the arguments advanced by Elowitz et al. (2021) identifying hydrazine monohydrate as plausible candidate to explain the absorption, with Titan as the potential source of the hydrazine monohydrate.

The Hapke model results presented in this work demonstrate a structural difference in the regolith when observed at low phase angles. The lack of data points at very small phase angles did not allow for strong quantitative constrains on the opposition effect. However, the Helene's phase curve at 610 nm shows a stronger opposition effect for phase angles smaller than 30°. The contrast in the slope of the opposition effect is a reflection of the differences observed in ISS images of Dione and Helene, showing a fluffier or finer grained regolith structure at Helene.

Helene's irregular shape, rotational period and small size render difficult the investigation of E-ring grains deposition and energetic particle bombardment on its surface. Umurhan et al (2015, 2021) reported that the surface has been heavily modified by mass flows. Activity on the satellite surface interferes with the analysis of space weathering on its surface, potentially erasing its effects. The moving material seems to brighten the surface (Hedman et al, 2020). Competitive hypotheses have been expressed to explain the brighter surface of Helene compared to Dione. Hedman et al. (2020) suggested it could either be due to an asymmetric flux of E-ring particles, or recent collisions with larger impactors. Umurhan et al. (2021) reported that the estimated rates of deposition at Helene derived from the current E-ring system are very low (Kempf et al., 2018) and they suggest alternative sources such as cryovolcanic or impact-generated debris from Dione or Tethys, or a catastrophic recent event in the inner satellite system of Saturn to explain the presence of the bright mass flows on Helene's leading side. The ωP(0) value we derived in this work is coherent with the visually bright and smooth aspect of Helene's LH and with resurfacing/landslide events, but is not indicative of an exogenic or endogenic origin. Coating by E-ring grains only is most likely unable to reproduce the ωP(0) value observed at Helene and Dione, because the higher value at Dione might be driven by the greater surface area of Dione relative to Helene. Other mechanism are thus required to brighten Helene's surface. For this reason, we favor the impact hypothesis to explain Helene's photometric behavior. Following up on the hypothesis of the Moon's formation, we suggest that Helene could have formed as a consequence of a giant impact on Dione. A better understanding of Dione's interior structure and overall composition (acquired through a dedicated spacecraft mission) and the identification of the water-ice contaminant(s) in the Saturn system (acquired via further laboratory experiment on ices) would allow us to verify if Helene's and Polydeuces (the other Lagrangian satellite of Dione) surfaces' composition are representative of Dione 'crust'.

Conclusion

We analyzed multi-wavelength datasets of Helene leading hemisphere, from 110nm up to 5μm, using quasi-simultaneous observations from the UVIS, ISS and VIMS instrument taken on the same day. We completed the analysis with a water-ice modeling of Helene's FUV spectrum and with visible photometry of Helene and Dione at 610nm. We presented the first phase curve of Helene.

We found Helene to be brighter in the visible and darker in the FUV and near-IR. The spectral signature of water-ice is present in every wavelength domain, with the addition of an unidentified spectral signature around 185nm. However, laboratory studies are currently insufficient to determine the nature of the UV absorber(s).

Helene displays different opposition effect characteristics than Dione, Dione having a steeper opposition effect slope. However, the lack of data at low phase angle at Helene did not allow us to quantify the shadow-hiding and coherent backscattering opposition effect parameters with low uncertainty. Helene also shows evidence of different regolith structure in the FUV compared to Dione, which might be attributed to the mass flows observed on its leading hemisphere.

Declaration of Competing Interest

None

Acknowledgments

We thank the Cassini Data Analysis Program for their support of this work (NNH16ZDA001N-CDAP), as well as Mauro Ciarniello and Gianrico Filacchione for sharing VIMS data. Thank you to the reviewers for their constructive feedback

APPENDIX

Table A.1
List of Dione disk-integrated observations at 610nm.

Observation name	Phase angle (°)	Longitude (°W)	Latitude (°)
N1556135770_1_CALIB.IMG('CL1','CL2')	40.303	48.233	-52.504
N1721708079_1_CALIB.IMG('CL1','CL2')	5.494	49.39	17.359
N1820504440_1_CALIB.IMG('CL1','CL2')	152.608	102.279	-0.153
N1820504480_1_CALIB.IMG('CL1','CL2')	152.609	102.339	-0.15
N1820504528_1_CALIB.IMG('CL1','CL2')	152.61	102.408	-0.154
N1820505393_1_CALIB.IMG('CL1','CL2')	152.637	103.784	-0.16
N1514090211_1_CALIB.IMG('CL1','CL2')	27.908	105.018	-0.576
N1829283513_1_CALIB.IMG('CL1','CL2')	128.026	107.621	-1.511
N1660397694_1_CALIB.IMG('CL1','CL2')	148.979	116.557	-10.326
N1507717036_1_CALIB.IMG('CL1','CL2')	21.856	136.621	-0.501
N1544893295_1_CALIB.IMG('CL1','CL2')	80.717	139.728	34.053
N1581273972_1_CALIB.IMG('CL1','CL2')	18.723	147.263	-25.662
N1614266079_1_CALIB.IMG('CL1','CL2')	165.802	147.768	4.717
N1581274430_1_CALIB.IMG('CL1','CL2')	18.781	148.427	-25.516
N1646375000_1_CALIB.IMG('CL1','CL2')	72.414	152.078	0.365
N1581276833_1_CALIB.IMG('CL1','CL2')	19.242	154.556	-24.691

Table A.2
List of Helene disk-integrated observations at 610nm.

Observation name	Phase angle (°)	Longitude (°W)	Latitude (°)
N1519536732_1_CALIB.IMG('CL1','CL2')	97.357	110.655	-0.844
N1519537272_1_CALIB.IMG('CL1','CL2')	100.381	108.301	-0.724
N1563643679_1_CALIB.IMG('CL1','CL2')	64.283	356.45	-6.879
N1563644053_1_CALIB.IMG('CL1','CL2')	61.801	359.544	-7.025
N1606207298_1_CALIB.IMG('CL1','CL2')	31.376	94.308	46.183
N1606207385_1_CALIB.IMG('CL1','CL2')	30.396	93.982	45.025
N1606207404_1_CALIB.IMG('CL1','CL2')	30.18	93.911	44.766
N1606207423_1_CALIB.IMG('CL1','CL2')	29.964	93.84	44.504
N1606207442_1_CALIB.IMG('CL1','CL2')	29.747	93.769	44.241
N1606207594_1_CALIB.IMG('CL1','CL2')	27.997	93.206	42.05
N1606207803_1_CALIB.IMG('CL1','CL2')	25.542	92.443	38.79
N1606207879_1_CALIB.IMG('CL1','CL2')	24.637	92.169	37.531
N1606207993_1_CALIB.IMG('CL1','CL2')	23.269	91.76	35.567
N1606208050_1_CALIB.IMG('CL1','CL2')	22.581	91.558	34.551
N1606208126_1_CALIB.IMG('CL1','CL2')	21.659	91.289	33.16

N1675163339_1_CALIB.IMG('CL1','CL2')	87.885	255.668	-4.016
N1675163665_4_CALIB.IMG('CL1','CL2')	83.7	250*	-4*

*approximate. Data are missing from PDS

References

Brown, R.H., et al., 2004, The Cassini Visual and Infrared Mapping Spectrometer (VIMS) investigation. Space Sci. Rev. 115: 111-168

Buratti, B.J., Veverka, J., 1984. Voyager photometry of Rhea, Dione, Tethys, Enceladus and Mimas. Icarus 58, 254–264.

Buratti, B., Mosher, J., Nicholson, P., McGhee, C., French, R., 1998. Near-infrared photometry of the saturnian satellites during ring plane crossing. Icarus 136, 223–231.

Burns, J.A., in Satellites, J. A. Burns, M. S. Matthews, Eds. (Univ. of Arizona Press, Tucson, AZ, 1986), pp. 1–38

Domingue, D., Hapke, B., Lockwood, G., Thompson, D., 1991. Europa's phase curve: Implications for surface structure. Icarus 90, 30–42.

Elowitz, M., Sivaraman, B., Hendrix, A. Lo, J-I, Chou, S-L., Cheng, B-M., Sekhar, R. and N.J. Mason (2021), Possible detection of hydrazine on Saturn's moon Rhea, Science Adv. 2021; 7 : eaba5749

Esposito, L.W. et al., 2004. The Cassini ultraviolet imaging spectrograph investigation. Space Sci. Rev. 115, 299–361.

Filacchione, G. and 18 coauthors (2012), Saturn's satellites and rings investigated by Cassini-VIMS III - radial compositional variability, Icarus 220, 1064-1096

Flasar, F.M., Kunde, V.G., Abbas, M.M., Achterberg, R.K., Ade, P., Barucci, A., B´ezard, B., Bjoraker, G.L., Brasunas, J.C., Calcutt, S.B., Carlson, R., C´esarsky, C.J., Conrath, B.J., Coradini, A., Courtin, R., Coustenis, A., Edberg, S., Edgington, S., Ferrari, C., Fouchet, T., Gautier, D., Gierasch, P.J., Grossman, K., Irwin, P., Jennings, D.E., Lellouch, E., Mamoutkine, A.A., Marten, A., Meyer, J.P., Nixon, C.A., Orton, G.S., Owen, T.C., Pearl, J.C., Prang´e, R., Raulin, F., Read, P.L., Romani, P.N., Samuelson, R.E., Segura, M.E., Showalter, M.R., Simon-Miller, A.A., Smith, M.D., Spencer, J.R., Spilker, L.J., Taylor, F.W., 2004. Exploring the Saturn system in the thermal infrared: the composite infrared spectrometer. Space Science Rev. 115, 169–297. https://doi.org/10.1007/s11214-004-1454-9.

Hapke, B., 2012. Theory of reflectance and emittance spectroscopy, second ed. Cambridge University Press.

Hedman, M.M., Helfenstein, P., Chancia, R.O., Thomas, P., Roussos, E., Paranicas, C., Verbiscer, A.J, 2020. Photometric analyses of saturn's small moons: aegaeon, methone, and pallene are dark; helene and calypso are bright. Astron. J. 159 https:// doi.org/10.3847/1538-3881/ab659d.

Hendrix, A.R., Hansen, C.J., 2008. The albedo dichotomy of Iapetus measured at UV wavelengths. Icarus 193, 344–351.

Hendrix, A.R., Domingue, D.L., Kimberly, K., 2005. The icy Galilean satellites: Ultraviolet phase curve analysis. Icarus 173, 29–49.

Hendrix, A.R., Filacchione, G., paranicas, C., Schenk, P. and Scipioni, F. 2018. Icy Saturnian Satellites: Disk-Integrated UV-IR characteristics and links to exogenic processes, Icarus 300, 103-114, http://dx.doi.org/10.1016/j.icarus.2017.08.037

Howett, C.J.A., Royer, E., 2021. Constraining the surface properties of Helene. Icarus. https://doi.org/10.1016/j.icarus.2021.114366.

Kempf, S., Horanyi, ´ M., Hsu, H.-W., Hill, T.W., Juh´ asz, A., Smith, H.T., 2018. Saturn's diffuse E Ring and Its connection with Enceladus. In: Schenk, P.M., et al. (Eds.), Enceladus and the Icy Moons of Saturn. University of Arizona Press, Tucson, pp. 195–210.

Miller, E, Klein, G., Juergens, D., Mehaffey, K., Oseas, J., Garcia, R., et al.: 1996, SPIE 2803, 206.

Nelson, R.M., Lane, A.L., Matson, D.L., Veeder, G.J., Buratti, B.J., Tedesco, E.F., 1987. Spectral geometric albedos of the Galilean satellites from 0.24 to 0.34 micrometers: Observations with the international ultraviolet explorer. Icarus 72, 358–380.

Pipes, J.G.; Browell, E.V. and Anderson, R.C. (1974), Reflectance of amorphous-cubic NH3 frosts and amorphous-hexagonal H2O frosts at 77K from 1400 to 3000Å, Icarus, Vol. 21, 283-291

Porco, C. C. and 19 co-authors (2004), Cassini imaging science: instrument characteristics and anticipated scientific investigations at Saturn. Space Sci. Rev. 115: 363-497

Royer, E.R. and Hendrix, A.R. (2014), First far-ultraviolet disk-integrated phase curve analysis of Mimas, Tethys and Dione from the Cassini-UVIS data sets, Icarus, Vol. 242, 158-171

Royer, E.R, Espositio, L.W. and Elliott, J. (2019), Mapping of the 185 nm absorption feature on the icy satellites of Saturn, LPSC abstract #1824

Thomas, P., Helfenstein, P., 2019. The Small Inner Satellites of Saturn: Shapes, Structures and some Implication. Icarus.

Thomas, P., Tiscareno, M.S., Helfenstein, P., 2018. The inner small satellites of Saturn, and Hyperion. In: Schenk, P., Clark, R., Howett, C.J.A., Verbiscer, A., Waite, J.H., Dotson, R. (Eds.), Enceladus and the Icy Moons of Saturn. University of Arizona Press, pp. 387–408.

Thomas, P., Helfenstein, P., 2019. The small inner satellites of Saturn: shapes, structures, and some implications. Icarus. https://doi.org/10.1016/j.icarus.2019.06.016.

Thomas, P.C., Burns, J.A., Hedman, M., Helfenstein, P., Morrison, S., Tiscareno, M.S., Veverka, J., 2013. The inner small satellites of Saturn: a variety of worlds. Icarus. 226, 999–1019. https://doi.org/10.1016/j.icarus.2013.07.022. Turcotte, D.L., Schubert, G., 2014. Geodynamics. Cambridge University Press,

Umurhan, O.M., Howard, A.D., Moore, J.M., Schenk, P.M., White, O.L., 2015. Reconstructing Helene's surface history, plastics and snow. In Lunar and Planetary Science XLVI, Abstract #2400. Lunar and Planetary Institute, Houston.

Orkan M. Umurhan a,b,* , Alan D. Howard c , Oliver L. White a,b , Paul M. Schenk d , Jeffrey M. Moore (2021), Modeling global-scale mass flows on the Lagrangian satellites of Dione and Tethys, Icarus, vol. 369 – 114612

Verbiscer, A., 2007. R. French, M. Showalter and P. Helfenstein. Enceladus: cosmic graffiti artist caught in the act. Science 315, 815.

Verbiscer, A., Helfenstein, P., Buratti, B., Royer, E., 2018. Surface properties of Saturn's moons from optical remonte sensing. In: Schenk, P., Clark, R., Howett, C.J.A., Verbiscer, A., Waite, J.H., Dotson, R. (Eds.), Enceladus and the Icy Moons of Saturn. University of Arizona Press, pp. 323–341

Warren, S.G., Brandt, R.E., (2008), Optical constants of ice from the ultraviolet to the microwave: A revised compilation. J. Geophys. Res. 113. D14220. doi:10.1029/ 2007JD009744.

Warren, S.G., (1984), Optical constants of ice from the ultraviolet to the microwave. Appl. Opt. 23, 1206–1225

West, R., Knowles, B., Birath, E., et al. 2010, P&SS, 58, 1475